Detrimental effect of high-productivity L-PBF parameters on metal dusting resistance of Inconel 625

A. Vernouillet [a,*], A. Vande Put [a], A. Pugliara [a,b], E. Epifano [a], T. De Terris [c], P. Peyre [c], S. Doublet [d], D. Monceau [a]

[a] CIRIMAT, ENSIACET, Université de Toulouse, CNRS, BP 44362, 31030, Toulouse Cedex 4, France
[b] Centre de Microcaractérisation Raimond Castaing, Université Toulouse 3 Paul Sabatier, Toulouse INP, INSA Toulouse, CNRS, Université de Toulouse, Espace Clément Ader, Toulouse 31400, France
[c] Laboratoire PIMM, UMR 8006 Arts et Métiers-CNRS-CNAM, HESAM Université, 151 Bd de l'Hôpital, Paris 75013, France
[d] Air Liquide R&D, Centre de Recherche Paris Innovation Campus, 1 chemin de la porte des loges, BP-126, Jouy-en-Josas Cedex 78354, France

ARTICLE INFO

Keywords:
Metal dusting corrosion
Additive manufacturing
Nickel-Based Superalloys
Highproductivity
Process parameters

ABSTRACT

The effect of increased productivity in L-PBF manufacturing on the metal dusting resistance of Inconel 625 was studied at 610 °C. Two sets of processing parameters were tested: the standard parameters given by the machine manufacturer and degraded parameters with increased scan speed and hatching distance. The materials obtained with degraded parameters presented numerous lacks of fusion at the surface and exhibited significantly shorter incubation times before corrosion. Carburisation was preferentially localised around the defects where the oxide scale was less protective and where the confinement of the atmosphere could result in an increase of the local carbon activity.

1. Introduction

Metal dusting is a catastrophic form of corrosion which was first encountered in the petroleum industry [1] during the production of butadiene from naphta and more recently in hydrogen production [2]. Indeed, hydrogen is industrially produced from the steam methane reforming (SMR) or partial oxidation (POX) processes and the water gas shift reaction. This leads to the formation of co-products, CO and CO_2. The cooling of the resulting gas mixture composed of H_2, CO, CO_2, CH_4 and H_2O, exposes the iron- and nickel-based alloys to metal dusting. It is frequently observed in steam reforming processes in all plant parts, in particular equipment parts of the waste heat section located downstream of the SMR or POX unit, that come into contact with the synthesis gas produced between 400 °C and 800 °C. This results in high maintenance costs and can lead to serious safety issues, such as ruptured pipes and pressure vessels and/or leaks of toxic carbon monoxide. This particular form of corrosion by carbon takes place between 400 °C and 800 °C, in highly carburising atmospheres (carbon activity $>> 1$) [3,4]. In this type of gaseous atmosphere, the oxygen partial pressure is extremely low (typically around 10^{-24} bar). It leads to the disintegration of the metallic alloy into a dust composed of carbon and fine particles of metals, carbides and oxides. When alloys form a protective oxide layer on the surface, metal dusting results into pits, forming from the oxide scale defects.

To intensify the production of small volumes of hydrogen for hydrogen mobility, and for a wide range of processes, heat exchanges have to be maximised in smaller reactors. This implies designing a counter-current reactor with very thin walls. Additive manufacturing techniques such as powder bed fusion (PBF) allows the construction of intricate geometries: a powder bed is melted in a predetermined pattern using a laser (L-PBF) or an electron beam, another layer of powder is then deposited on top of the first one and the part is built layer by layer [5,6].

This work focuses on the metal dusting behaviour of Inconel 625 obtained by L-PBF. Conventionally manufactured Inconel 625 has a good metal dusting resistance [7,8]. However, several studies have shown that the manufacturing process has an influence on the oxidation and corrosion behaviours of nickel-based alloys. Hong *et al.* studied the oxidation behaviour of Inconel 625 obtained by powder-based direct energy deposition, which is an additive manufacturing technique, and subsequently ground [9]. The oxidation kinetic was faster than for conventionally manufactured samples. However, the nature of the oxide

* Corresponding author.
E-mail address: annabelle.vernouillet@proton.me (A. Vernouillet).

was unchanged. Pineda-Arriega *et al.* also showed that additive manufactured Inconel 625 presented faster oxidation kinetics but identical corrosion products compared to conventionally manufactured Inconel 625 [10]. On the contrary, for Inconel 718, Sanviemvongsak *et al.* showed that the oxidation kinetics were similar between L-PBF and wrought samples whether they were ground or not [11]. Also, they observed that electron beam melting manufactured Inconel 718 had faster oxidation kinetics but this was only due to the higher surface area [11]. A previous study at 610 °C showed the importance of the surface roughness resulting from the additive manufacturing of the samples and of the hot isostatic pressing (HIP) treatment on the metal dusting behaviour of Inconel 625 [12]. The roughness of the samples and the coarse microstructure obtained after the HIP treatment favoured the formation of non-protective spinel oxides. Therefore, the incubation time for the additive manufactured samples was significantly reduced to around 6 000 h [12]. This is much shorter than the incubation time of 13 500 h observed by Fabas *et al.* for conventionally manufactured samples exposed to similar metal dusting conditions (high H_2O content, high total pressure) at 570 °C [8]. Other effects of additive manufacturing on cyclic oxidation or intergranular oxidation, for example, were recently reviewed by Monceau and Vilasi [13]. Moreover, numerous additive manufacturing parameters can be adjusted and have a strong influence on the material obtained. Process parameters such as scan speed (S), laser power (P), layer thickness (T) and hatching distance (H) to only cite a few examples can indeed modify the microstructure [14] and the density [15] of the material. Jia and Gu studied the oxidation of additive manufactured Inconel 718, ground using SiC abrasive paper (1 000 grit), during 100 h, under air [16]. They showed that an increase in volumetric energy density (laser power over scan speed) decreased the oxidation parabolic constant. When parts have to be produced commercially, it is necessary to know what can be done in terms of productivity without degrading the durability of the parts. This work therefore focuses on the influence of process parameters such as scan speed and hatching distance on the metal dusting behaviour of Inconel 625.

2. Materials, experimental procedure and computational methods

All the samples tested were made of Inconel 625. The chemical composition in atomic percent of both the wrought and additively manufactured samples is presented in Table 1. One can notice that the two compositions are similar, except the level of Ti impurity which is much higher in the wrought alloy. This is an element which can form internal oxides and carbides. The level of Nb is also higher in the wrought alloy. Nb oxides are very stable and have already been observed in the internal part of oxide scales in additive manufactured Inconel 625 [17] and Inconel 718 [18,19].

Two sets of parameters for additive manufacturing were studied in this work. The first batch of samples was manufactured with the following parameters: the scan speed for filling parameters was 650 mm/s, the hatching distance 140 μm and for the contour the scan speed was 300 mm/s as given in [20]. The second batch was manufactured by the PIMM laboratory (Paris, France) on a SLM125 HL machine from SLM Solutions GmbH. For the second batch, the scan speed and the hatching distance were greatly increased to accelerate manufacturing. No contouring was applied which also decreased the manufacturing time. Several sets of parameters were tested in order to obtain samples with a reasonable density but exhibiting deteriorated surfaces (higher surface roughness and presence of numerous sub-surface defects in the alloy, which will be described below). These manufacturing conditions are called “degraded” parameters in the article. The values chosen for the scan speed and the hatching distance of the degraded parameters were 1 200 mm/s and 180 μm respectively. The samples with standard parameters were discs of 14 mm diameter, 2 mm thick and with a central hole of 2 mm diameter whereas the samples with degraded parameters had a rectangular shape ($23\times14\times1.8\,mm^3$ with a hole of 2 mm diameter).

Table 1
Chemical composition (at%) of the wrought and the as-built L-PBF samples.

at%	Ni	Fe	Cr	Nb	Mo	Ti	Al
L-PBF	62.7	4.2	24.9	2.1	5.9	0.1	0.1
Wrought	61.3	4.2	24.6	3.7	5.6	0.5	0.1

After additive manufacturing, all the samples underwent a residual stress relief heat treatment at 975 °C, under argon for 30 min. Some of the samples also underwent an HIP treatment, common in additive manufacturing to increase the density of the parts. This treatment (1150 °C, under 1020 bar of argon for 3 h) was done by Bodycote (Magny-Cours, France).

Four systems were tested in total (12 samples): L-PBF and L-PBF + HIP with standard and degraded parameters. The systems will be described as L-PBF - standard, L-PBF + HIP - standard, L-PBF - degraded and L-PBF + HIP - degraded, as described in Fig. 1. Before placing them in the corrosion rig, the samples were cleaned for two minutes in ultrasonic ethanol, weighed, measured and photographed. They were then positioned on the horizontal alumina sticks of the vertical alumina sample holder. Three samples for each system were placed in the vertical rig in order to evaluate the reproducibility of each system behaviour. Despite the metal dusting atmosphere being out of equilibrium, a previous study showed that the metal dusting resistance did not depend on the position of the sample in the furnace (upstream or downstream) [12]. Every 500 h, the samples were taken out of the rig to be cleaned, weighed and photographed. After 2 000 h, one sample was definitely taken out of the rig to carry out destructive metallurgical characterisations.

The corrosion of these various samples was carried out in a rig where the industrial conditions resulting in metal dusting were reproduced. The temperature was set at 610 °C because it is in the most critical temperature range for nickel-based alloys [21,22]. The total pressure inside the rig was 16 bars. The gas molar composition was as follows: 48%H_2-9%CO-6%CO_2-3%CH_4-34%H_2O and the gas velocity at 610 °C was equal to 0.003 $m.s^{-1}$. The carbon activity ($a_C = 6.9$) and the oxygen partial pressure (1.8×10^{-24} bar) were calculated based on the reaction of reduction of CO (R1) and the water decomposition reaction (R2) respectively, using the Eqs. (1) and (2) and considering an ideal gas behaviour:

$$CO + H_2 = C + H_2O \quad (R1)$$

$$H_2O = H_2 + ½\ O_2 \quad (R2)$$

$$aC = \frac{P_{CO} \times P_{H2}}{P_{H2O}} \times \exp\left(\frac{-\Delta G1}{RT}\right) \quad (1)$$

with P_{CO}, P_{H2}, P_{H2O} the partial pressures of carbon monoxide, dihydrogen and water vapour respectively, ΔG1 the Gibbs free energy of reaction (R1), R the ideal gas constant and T the temperature,

$$P_{O_2} = \left(\exp\left(\frac{-\Delta G2}{RT}\right) \times \frac{P_{H_2O}}{P_{H_2}}\right)^2 \quad (2)$$

with P_{O2}, the partial pressure of dioxygen, ΔG2 the Gibbs free energy of reaction (R2).

The molar Gibbs free energy changes associated to reactions 1 and 2 were calculated in J/mol using: −134515+142.37 T and 246440–54.8 T, respectively with T in K [23].

Gas analyses were performed at the outlet of the rig to verify the gas composition, as published in a previous study [12]. Moreover, previous studies showed that the position of the samples in the rig did not affect the metal dusting resistance [8,12]

Surface topographies were analysed using an interferometric and focus-variation microscope (Sensofar S neox, mag 10X and 1 μm of

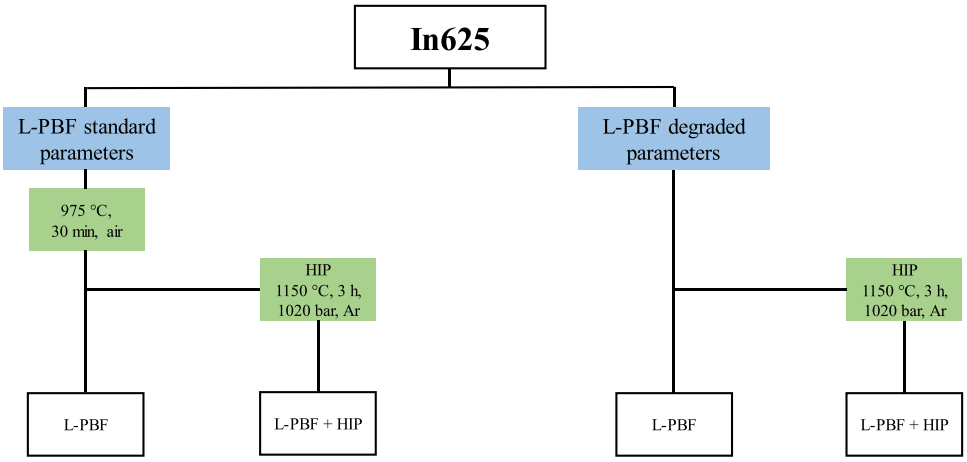

Fig. 1. Summary of the studied systems.

vertical resolution). The roughness parameter used here was the quadratic mean and was calculated from a 3D surface and not a 2D profile, according to Eq. (3). It corresponds to the standard deviation of the height distribution.

$$Sq = \sqrt{\frac{1}{A}\iint Z^2(x,y)dxdy} \quad (3)$$

With A the analysed area, Z the height function and x and y the coordinates.

Before and after exposure to the metal dusting atmosphere, XRD and Raman spectroscopy were performed to characterise the phases present in the alloy as well as the corrosion products (carbides and oxides). XRD was performed on a Brucker D8–2 apparatus, in theta-theta configuration with a copper source. The step was of 0.4° and the time by step of 1 s. Raman spectroscopy and fluorescence spectroscopy were carried out on a Labram HR800 Yvon Jobin spectrometer with a wavelength of 532 nm. Scanning electron microscopy (SEM) observations of the sample surface and cross section were performed on a field emission gun (FEG) scanning electron microscope Ultra55 Zeiss using secondary and backscattered electron modes (SE and BSE modes respectively). Transmission electron microscopy (TEM) samples were prepared using the Focused Ion Beam (FIB)-lift out technique in a THERMO FISHER NanoLab HELIOS 600i FIB / SEM. These samples were analysed on a transmission electron microscope JEOL JEM-2100 F operated at 200 kV, equipped with an energy dispersive X-ray spectroscopy (EDX) analyser Brucker SDD Xflash 5030, in high resolution (HR)-TEM, selected area electron diffraction (SAED) and scanning TEM (STEM)-EDX modes. Finally, microstructures were studied by electron backscatter diffraction (EBSD) characterisation with a FEG scanning electron microscope JEOL JSM 7100 F operated at 20 kV equipped with an EBSD Aztec HKL Advanced Nordlys Nano analyser. XRD diffractograms and electron diffraction were identified using Ca.R.Ine software.

Thermodynamic and kinetic calculations for the alloy were carried out using Thermo-Calc™ and DICTRA™ softwares, with the TCNI9 and MOBNI5 databases respectively. Thermodynamic and kinetic calculations were made to compare the theoretical carburisation depth with the experimental observations. For the carburisation simulation, the same approach presented by A. Engstrom *et al.* [24] was here applied. The δ phase was not included in the simulation because carbon is not described in the thermodynamic model of this phase, hence its presence would not have a significant effect on the simulation of carbon diffusion. The γ-matrix composition obtained by the thermodynamic calculations was entered as the global composition in the DICTRA simulation. The $M_{23}C_6$ phase, the only carbide predicted by thermodynamic computations for the system of interest, was entered as a spheroid phase. The dispersed system model was used, with a labyrinth function taking into account the impeding effect of the dispersed phase on diffusion. The diffusion within the carbides was considered negligible. The carbon activity (relative to graphite) was set equal to 1 at the surface of the alloy, for the entire simulation time, as a boundary condition. For all the metallic elements, zero-flux boundary conditions were set.

3. Results

3.1. Systems before exposure to metal dusting

Systems manufactured using standard parameters were previously characterised and tested under metal dusting conditions [12]. A few characterisation results of these systems are presented here for comparison with the systems manufactured with degraded parameters.

The metallographic cross-section of each system described previously is presented Fig. 2. It can be seen than the samples manufactured using the standard parameters exhibited a lower surface corrugation than the degraded samples while the high scan velocity and the large hatching distance (of the degraded parameters) created numerous defects on the sample surface. A surface defect or alloy defect (as indicated by arrows in Fig. 2) is here defined at the micrometric scale as an open pore in the alloy. These are likely lacks of fusion nearby the surface due to poor remelting of the adjacent laser melting bead because of higher scan velocity and wide hatching distance. It is quantified in 2D, using OM and SEM cross-sections. A dotted line is drawn (Fig. 2) on the theoretical surface to measure the width and depth of each defect. Each lack of matter below the line is considered as a defect at the surface of the alloy.

A statistical analysis on a length of 3 cm showed that there were approximately 4 alloy defects by millimetre along the observed cross-section for all systems which did not undergo HIP (250 μm in average between defects). However, the depth of these alloy defects was very different between the systems manufactured with standard and degraded parameters. The mean depth of the alloy defects on the L-PBF-standard samples was of 15 μm +/- 6 μm whereas the depth of the alloy defects on the systems manufactured with degraded parameters mainly ranged between 30 and 200 μm. Also, more visibly closed pores were observed within the bulk of the L-PBF-degraded sample on the optical image cross-section. Of course, 3D characterisation could reveal whether these apparently close pores are in fact connected to the surface. At this stage it is not known.

The density (measured using Archimedes' method) of the L-PBF – standard system was 8.40 +/- 0.01 $g.cm^{-3}$ and the density of the systems obtained with degraded parameters was 8.38 +/- 0.02 $g.cm^{-3}$. These density values are very close to the density of conventional (wrought) In625, equal to 8.44 $g.cm^{-3}$. This confirms that the samples

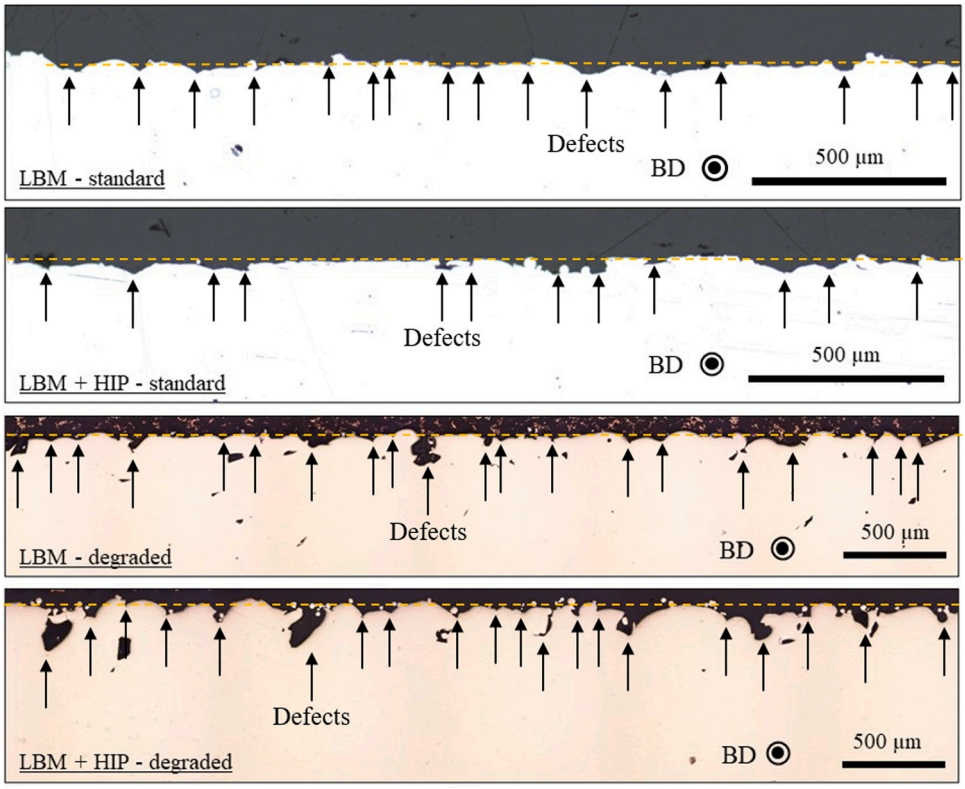

Fig. 2. Optical observation of a cross section of the standard (L-PBF(L-PBF and L-PBF + HIP) and degraded (L-PBF and L-PBF + HIP) systems, BD: building direction during the L-PBF process.

contain only a very small proportion of closed pores (resp. 0.4–0.6 vol% and 0.5–0.9 vol%).

After the HIP treatment, for both standard and degraded parameters, no closed pores were observed in cross sections, thus confirming the role of this high pressure treatment. Moreover, the number of alloy defects per mm decreased from 4.0 to 3.2 for the standard system and from 4.0 to 3.3 for the samples manufactured with degraded parameters. Surprisingly, it therefore seems that the HIP slightly decreases opened porosity. The surface roughness (Sq) measured with a confocal microscope on both degraded systems (L-PBF and L-PBF + HIP), using Eq. (3), was much higher than for the samples produced with standard parameters, respectively 33 +/- 3 µm compared to 11 +/- 1 µm.

This higher surface roughness increases the developed surface in contact with the metal dusting atmosphere. For the standard parameters, the real cross-section length is calculated by considering the alloy defects as grooves in 3D (described in a previous study [12]), and therefore triangles in two dimensions, perpendicular to the building direction, Fig. 3.

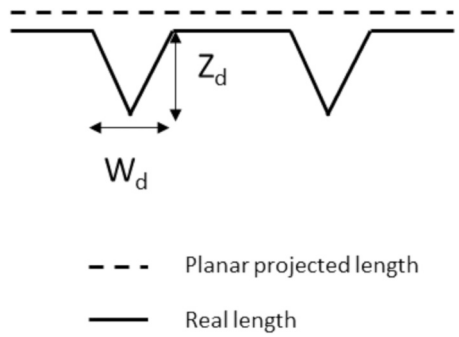

Fig. 3. Schematic of the surface of the sample in 2D, with W_d the mean width of the defects and Z_d the mean depth of the defects.

For 1 mm of planar projected length, the actual length is calculated using Eq. 4:

$$L_r = L_{pp} + D\left(2 \times \sqrt{\left(\frac{W_d}{2}\right)^2 + Z_d^2} - W_d\right) \quad (4)$$

With L_r the real length, L_{pp} the planar projected length, D the mean number of defects for the considered planar projected length, W_d the width of the defects measured on the sample surface and Z_d the mean depth of the defects. For standard parameters, the real surface is 1.04 times higher than the planar projected surface.

For the samples manufactured with degraded parameters, the defects are considered as cones with a square layout. The real surface for 1 mm^2 of planar projected surface is calculated using Eq. (5):

$$S_r = 1 - D^2 \times \pi \times \left(\frac{W_d}{2}\right)^2 + D^2 \times \pi \times \frac{W_d}{2} \times \sqrt{\left(\frac{W_d}{2}\right)^2 + Z_d^2} \quad (5)$$

For the samples manufactured with degraded parameters, the real surface is 1.16 (L-PBF) and 1.12 (L-PBF+HIP) times higher than the planar projected surface.

The surface exposed to the metal dusting atmosphere is therefore higher for the samples manufactured with degraded parameters than for samples obtained with standard ones.

As it can be seen on the Fig. 4, both L-PBF samples, manufactured with standard and degraded parameters, showed similar diffractograms: only the γ matrix was detected. The L-PBF + HIP samples, manufactured with standard and degraded parameters also presented similar diffractograms. In addition to the γ matrix, small peaks at 35° and 41° were detected, which correspond to δ-Ni_3Nb precipitates. Whatever the parameters, the γ peaks were wider for the L-PBF system than for the L-PBF + HIP system. This is due to a Nb segregation in the interdendritic regions, as observed by SEM and EDX (Fig. 5.a and c). Such segregation is common in Inconel 625 manufactured with L-PBF [17,24–26]. Some

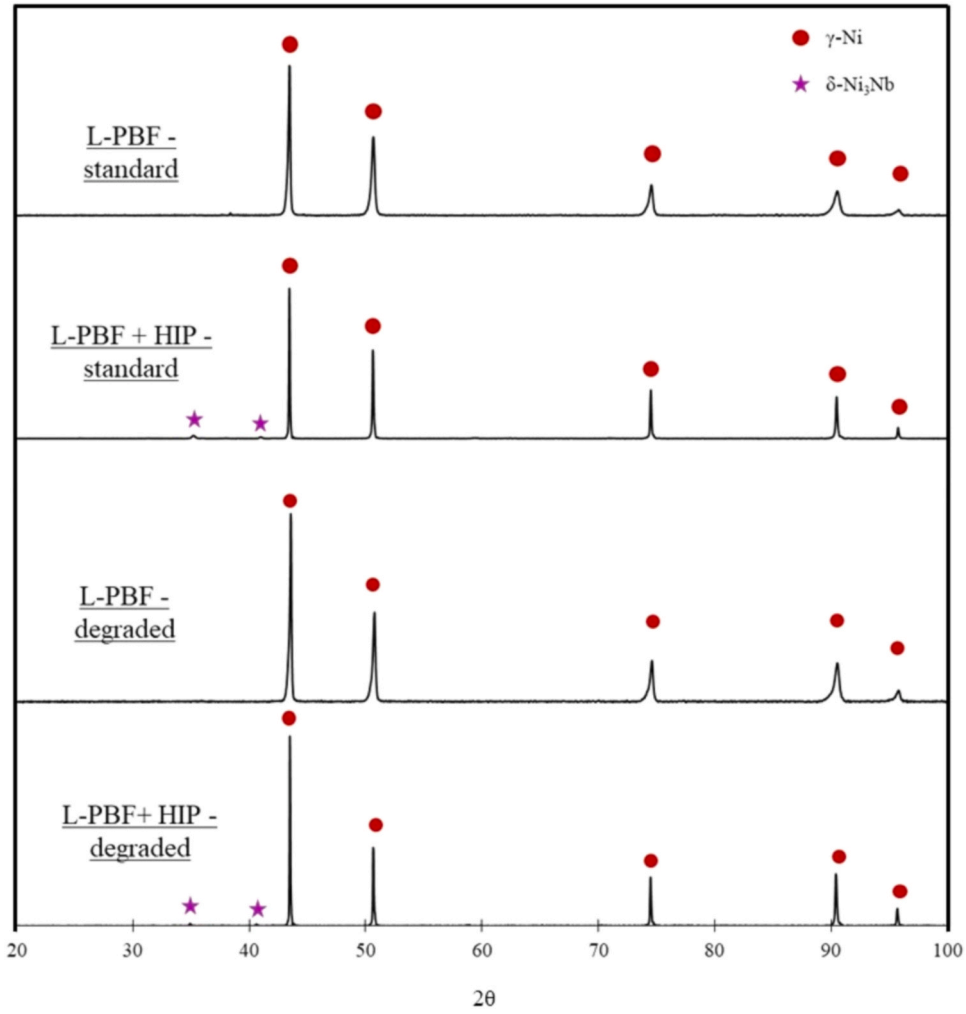

Fig. 4. XRD diffractograms of the L-PBF and L-PBF + HIP samples with standard and degraded parameters before exposure to metal dusting.

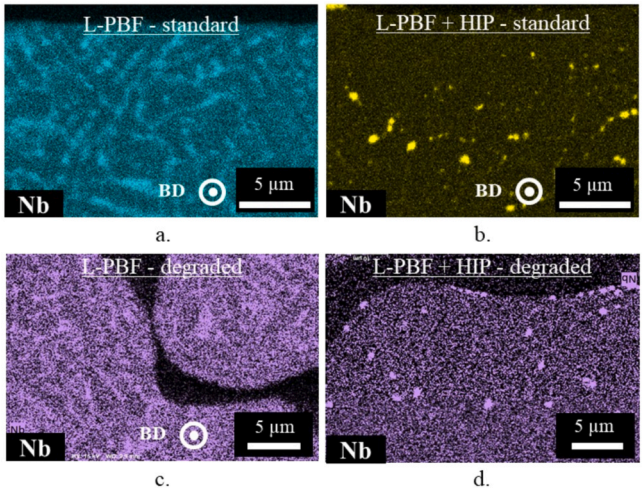

Fig. 5. Nb EDX maps of the cross-sections of the following systems close to the surface: a. L-PBF – standard, b. L-PBF + HIP – standard, c. L-PBF – degraded and d. L-PBF + HIP - degraded, BD: building direction.

authors considered this Nb segregation to be in the form of a Lava phase [20]. However, a phase in such high volume percentage would have been detected by XRD analyses. Therefore, it is here considered to be in the form of a Nb-rich γ-matrix which would explain the wider peaks observed in XRD for the L-PBF systems (obtained with standard and degraded parameters). During the HIP treatment, this Nb-segregation disappeared and was replaced by δ-Ni_3Nb precipitates, Fig. 5 (b and d), which were identified by XRD (Fig. 4).

A previous study showed that no continuous oxide layer was detected by SEM or XRD on the standard systems before exposure to the metal dusting atmosphere (Fig. 6. a. and b.): only alumina was detected locally by spectroscopy (based on the fluorescence of Cr^{3+} in alumina, measured using a laser in a Raman spectrometer) for both systems. The same observation was made on the samples obtained with degraded parameters, for which EDX analysis and fluorescence spectroscopy showed the local presence of alumina and probably of a Si-rich oxide on the L-PBF - degraded system (Fig. 6 c.1 and 2). The L-PBF + HIP - degraded system presented a non-continuous chromia scale and internal oxide precipitates rich in Al to a depth of 25 µm, Fig. 6.d. STEM-HAADF images and STEM-EDX mappings were performed to better understand the nature of the oxide in the alloy defects (open pores/lacks of fusion) of the L-PBF + HIP – degraded sample (Fig. 7). Only local chromium-enriched alumina was detected on the surface and identified by electron diffraction (not shown here), confirming the SEM observations. Alumina, when heated at temperatures above 1000 °C, can indeed contain chromium [27]. The internal oxidation was not precisely identified but the precipitates were rich in aluminium. Wagner's simplified oxidation model [23] was used to calculate the expected internal oxidation depth (X), after the HIP treatment at 1150 °C for 3 h, Eq. (6).

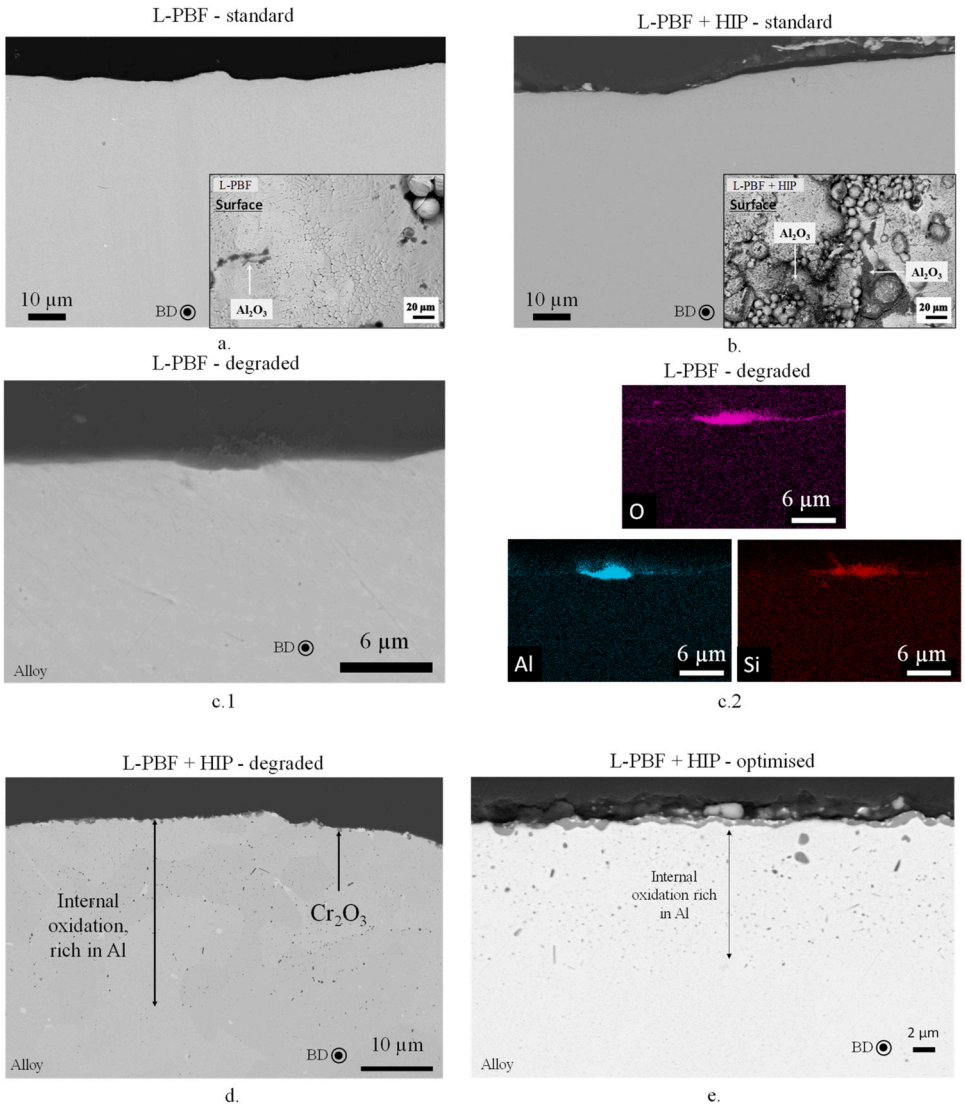

Fig. 6. Cross sections and surface SEM images (BSE mode) of a. L-PBF-standard system, b. L-PBF + HIP – standard system, c.1 L-PBF - degraded system, d. L-PBF + HIP - degraded system and e. L-PBF + HIP optimised system, before exposure to metal dusting, c.2 EDX mappings of c.1. BD: building direction.

$$X^2 = 2 \times k_p \times t \tag{6}$$

With k_p the parabolic kinetic constant ($m^2.s^{-1}$) determined by Eq. (7) and t the diffusion duration (s).

$$k_p = \frac{D_O \times N_O^{(s)}}{\nu \times N_{Al}} \tag{7}$$

With D_O the diffusion coefficient of oxygen in the Al and Cr depleted alloy matrix, $N_O^{(s)}$ the solubility limit of oxygen in the Al and Cr depleted γ matrix, ν the oxygen/metal ratio of Al_2O_3 and N_{Al} the aluminium concentration in the matrix below the internal oxidation zone. The internal oxidation depth, after the HIP treatment, was calculated by taking into account the equilibrium of the alloy surface with NiO on one hand and Cr_2O_3 on the other. The formation of NiO is the case that may result in the deepest internal oxidation, because it corresponds to the highest possible oxygen solubility limit in the metal matrix. It is here calculated to give a maximum value for the expected internal oxidation depth after the HIP treatment. For the equilibrium of the alloy with NiO, D_O and N_O were calculated using the equations in Park and Altstetter [28] at 1150 °C: 4.67×10^{-8} $cm^2.s^{-1}$ and 7.9×10^{-4} respectively. For the equilibrium of the alloy with Cr_2O_3, the same D_O was used and N_O was calculated, at 1150 °C, using Thermo-Calc to determine the concentration of oxygen in the γ phase when chromia first starts to form ($N_O = 7\times10^{-8}$). The calculated oxidation depth after the HIP treatment, in equilibrium with NiO, is 230 µm whereas it is only 0.7 µm when in equilibrium with Cr_2O_3.

The internal oxidation observed here is 30 µm deep. It is much higher than the calculated value in equilibrium with Cr_2O_3 indicating that internal oxidation started before the formation of the chromia scale. As previously explained, the value calculated in equilibrium with NiO may be considered as the maximum oxidation depth that can be observed. The fact that the measured depth is between the two calculated values is consistent with the formation of the internal oxidation during the HIP treatment. As no internal oxidation was observed on the L-PBF + HIP - standard samples it could therefore be deduced that the degraded parameters used to build the samples favoured this internal oxidation. However, internal oxidation was also observed on samples built with optimised parameters that are parameters resulting in almost no surface defects (Fig. 6.e). The internal oxidation observed on the samples obtained with degraded parameters is therefore not due to the parameters used during the additive manufacturing process but probably to the HIP conditions that can vary when performed at the industrial scale. Mrozowski *et al.* showed recently that the variability of the HIP conditions can influence the oxidation of the alloy during the HIP treatment [29].

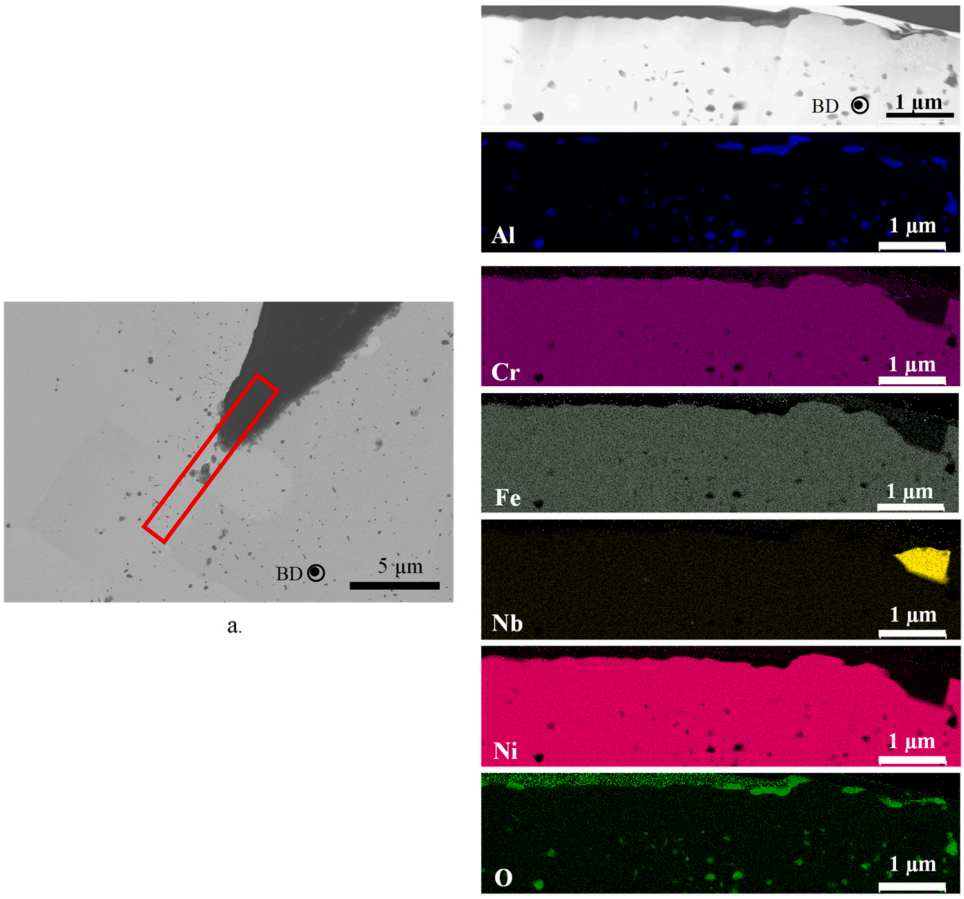

Fig. 7. a-SEM-BSE image of the cross-section of the L-PBF + HIP - degraded system before exposure to metal dusting (the red square indicates where the FIB lamella was taken), b- STEM-HAADF image and STEM-EDX maps of one area of the FIB lamella.

Fig. 8 shows EBSD-kernel average misorientation (KAM) maps of the four systems. KAM measures the local misorientation between a pixel and its neighbour, therefore indicating internal strain in the form of dislocation density (geometrical necessary dislocation (GND)). As detailed in a previous study [12], EBSD analyses of the L-PBF - standard system showed a very heterogeneous microstructure with small grains of approximately 10 µm in diameter near the surface (Fig. 8.a). A strong misorientation due to the fast cooling rates during the additive manufacturing process inducing residual thermal stresses after cooling was also detected. After the HIP treatment, performed at 1150 °C, the fine microstructure disappeared (Fig. 8.b). Large heterogeneous grains as well as twins formed and the deformation within the grains disappeared. This is in agreement with several studies that showed that recrystallisation occurs at temperatures higher than 1050 °C, when the dislocation density is high enough [30–32]. For the L-PBF - degraded system, a fine microstructure was also observed near the surface (a few micrometres in depth). The core microstructure of the L-PBF - degraded system was similar to the one already observed on the L-PBF standard system: large grains of approximately 15 µm wide and 70–80 µm long, separated by layers of smaller equiaxed grains. However, fewer local misorientations were detected on the L-PBF - degraded system than on the L-PBF - standard system. Moreover some misorientations (straight lines) observed on the L-PBF + HIP – degraded system could be due to scratches remaining from the polishing step rather than dislocation density. During the HIP treatment, large grains formed but the fine microstructure on the surface or along the defects remained. This less pronounced recrystallisation could be due to the lower dislocation density in the L-PBF - degraded system. Indeed, De Terris et al. showed that low energy parameters led to lower GND density and consequently slower recrystallisation during manufacturing by L-PBF [33].

Table 2 summarises the characterisations performed on the four systems studied here: L-PBF – standard, L-PBF + HIP – standard, L-PBF – degraded and L-PBF + HIP – degraded.

3.2. *Metal dusting degradation*

The mass variation of the systems obtained with standard and degraded parameters are presented Fig. 9.

The behaviour of the L-PBF - degraded system was more heterogeneous than the L-PBF - standard system as two samples of the degraded system drastically lost mass after 1 000 h whereas the mass loss of the third one was more gradual. However, the mass variations show that overall, the L-PBF - degraded system exhibited mass loss earlier than the standard systems: mass loss started after 1 000 h for the L-PBF degraded system versus 6 000 h for the L-PBF standard system. The appearance of the first pit is also an indicator of the quicker metal dusting degradation on the systems fabricated with degraded parameters. This parameter was followed at each removal of the samples from the rig, every 500 h, using a binocular magnifier. The first pit was observed after 1 500 h for the L-PBF degraded systems. It was only observed after 6 500 h for the L-PBF - standard system. For the L-PBF + HIP system, both systems had very heterogeneous behaviours. Two samples of the L-PBF + HIP – degraded system lost mass drastically after 1 000 h whereas the mass loss was more gradual for one of the L-PBF + HIP – standard samples and started after 6 500 h for another one. The first pit was observed after 1 500 h for the L-PBF + HIP – degraded system. However, the first pit was

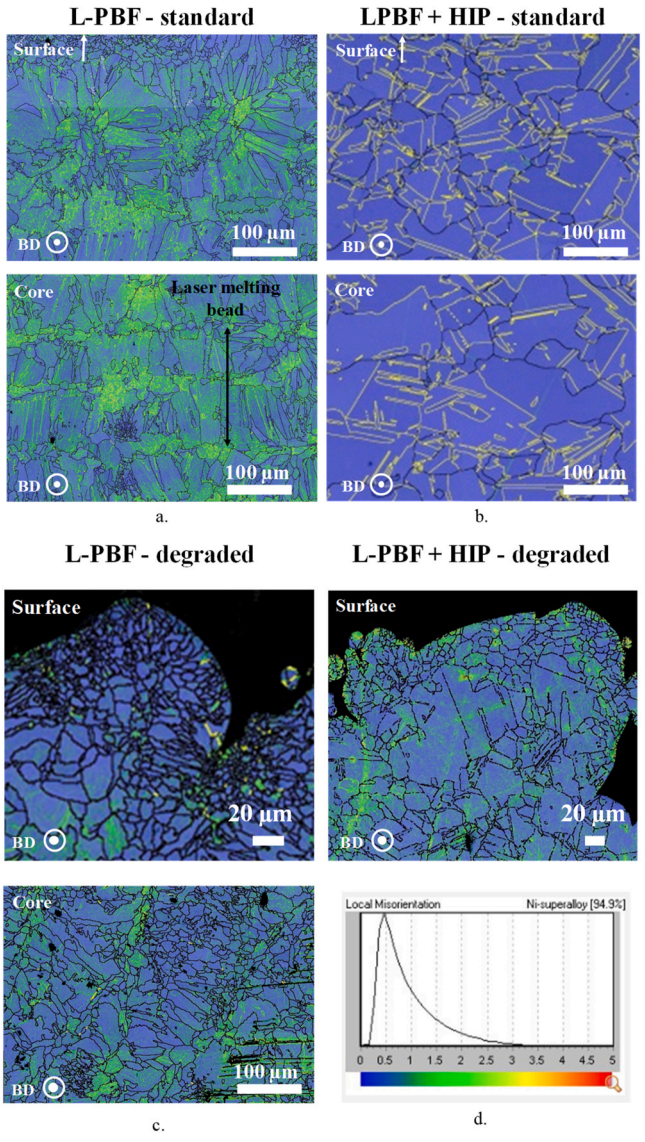

Fig. 8. EBSD – KAM maps of the cross-section of the a. L-PBF – standard system, b. L-PBF + HIP – standard system, c. L-PBF-degraded system and d. L-PBF + HIP - degraded system before exposure to the metal dusting atmosphere and local misorientation scale. BD: building direction.

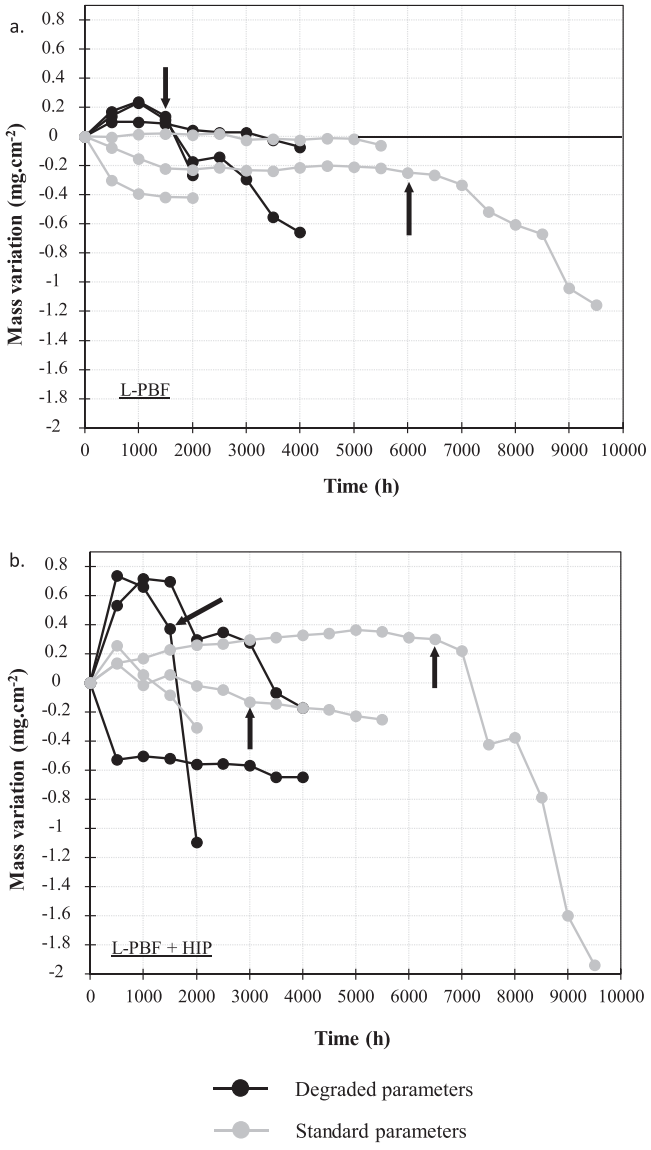

Fig. 9. Mass variation of systems obtained with standard and degraded parameters versus the time of exposure to the metal dusting environment. The arrows represent the time at which the first pit was observed.

Table 2
Summary of the L-PBF-standard, L-PBF-degraded, L-PBF + HIP-standard and L-PBF + HIP-degraded systems.

Parameters	System	Surface roughness	Microstructure at the surface	Grain size at the surface	Chemical segregation	Oxidation
Standard	L-PBF	Sq = 11 +/- 1 µm 4.0 defects /mm L_r = 1.04	Large deformation	At the surface 180 grain boundaries per mm	Nb segregation at the grain boundaries	Local presence of alumina No continuous oxide layer observed by SEM
	L-PBF + HIP		Recrystallisation and formation of twins No residual deformation	At the surface: 40 grain boundaries per mm	No Nb segregation Formation of Nb-rich precipitates	
Degraded	L-PBF	Sq = 33 +/- 3 µm 4.0 defects / mm L_r = 1.52	Deformation NOT localised around the defects	At the surface and along the defects: numerous small grains (ranging from 1 to 10 µm)	Nb segregation at the grain boundaries	Local presence of alumina and of an oxide rich in Si No continuous oxide layer observed by SEM
	L-PBF+ HIP	Sq = 33 +/- 3 µm 3.3 defects / mm L_r = 1.25	Slight recrystallisation	At the surface: presence of small grains, a few micrometres in diameter	No Nb segregation Formation of Nb-rich precipitates	No continuous chromia and alumina layers and internal oxidation (oxides rich in Al)

detected after 3 000 h for one of the L-PBF + HIP - standard samples and after 6 500 h for the other sample. These results show a significant decrease in the incubation time for the systems fabricated using degraded parameters.

One sample of each system was characterised after 2 000 h of exposure to the metal dusting atmosphere, Fig. 10. Only minor carburisation was observed on the L-PBF - standard system. Homogeneous carburisation was detected on the L-PBF + HIP - standard sample. It was detailed in a previous study that the L-PBF + HIP - standard system presented a continuous chromia layer of approximately 500 nm after 2 000 h of exposure to the metal dusting atmosphere at 610 °C [12]. It was therefore suggested that the continuous nature of the observed oxide scale implied that the carburisation occurred before the formation of a continuous oxide scale of a sufficient thickness. The carbides observed on the standard systems were identified in a previous study as $Cr_{23}C_6$ and Cr_7C_3 [12]. Carburisation of the systems fabricated with degraded parameters was severe. In the case of the L-PBF – degraded system, carburisation was more pronounced around the defects. On the L-PBF + HIP - degraded system intergranular carburisation was observed on the whole surface. Intragranular carburisation was mainly observed around the surface defects and 85% of these defects presented both intergranular and intragranular carburisation. The localised nature of intragranular carburisation, around the defects, implies that the metal dusting degradation was more severe in these areas.

4. Discussion

The observations described previously lead to several conclusions:

- L-PBF – standard samples present less carburisation than L-PBF + HIP – standard samples [12]
- The defect-free areas (no open porosity at the metal surface) of the L-PBF – degraded samples present more carburisation than the L-PBF – standard samples,
- The defect areas at the surface of both the L-PBF and the L-PBF + HIP samples obtained with degraded parameters present more carburisation than the defect-free areas.

A carburisation simulation of the alloy was performed using the DICTRA software, according to the hypothesis and models detailed in Section 2. After 2 000 h, the calculated carburisation depth is 62 µm whereas the measured carburisation depth is approximately 25 µm for the L-PBF + HIP – standard sample and 50 µm for both the L - PBF – degraded and L-PBF + HIP – degraded samples. The lower carburisation depth observed for the L-PBF + HIP - standard sample confirms that the carburisation did not occur for the entire duration of 2 000 h of the experiment but only until the formation of a continuous and protective oxide scale. However, for the samples obtained with degraded parameters, the observed carburisation depth is close to the calculated one suggesting that carburisation occurred for the whole duration of the experiment, i.e. the oxide scale, if any, formed on these samples was not protective against carburisation.

An explanation was proposed in a previous publication for the increased carburisation of the L-PBF + HIP - standard samples compared to the L-PBF – standard samples. It was proposed that the recrystallisation due to the HIP treatment coarsened the grain size (Table 2) and reduced the number of dislocations which decreased the Cr diffusion fast paths, leading to the formation of a non-protective oxide scale ($FeCr_2O_4$) [12].

The defect-free areas (no open pores/lack of fusion) at the surface of the L-PBF - degraded samples are more carburised than the L-PBF - standard samples probably because there are less dislocations present in the L-PBF - degraded system (Fig. 8). As previously mentioned, the dislocations act as fast diffusion paths for the Cr. A lower dislocation density leads to the formation of non-continuous chromia scale on the defect-free areas as observed on Fig. 11. By modifying the microstructure and the level of residual internal stresses, the additive manufacturing parameters have an influence on the metal dusting degradation, even on the defect free areas.

Concerning the greater metal dusting degradation observed in the defects of the systems obtained with degraded parameters compared to the defect-free areas, several hypotheses can be made.

The first hypothesis is that the defects could act as a confined space, decreasing the renewal of the gaseous atmosphere, as proposed by Fabas *et al.* in cracks [34]. As oxide forms, the local oxygen partial pressure decreases therefore increasing the carbon activity. As detailed in Section 2 the carbon activity is calculated from Eq. (1).

Using Eq. 1 and Eq. 2, the carbon activity can be expressed with the Eq. (8):

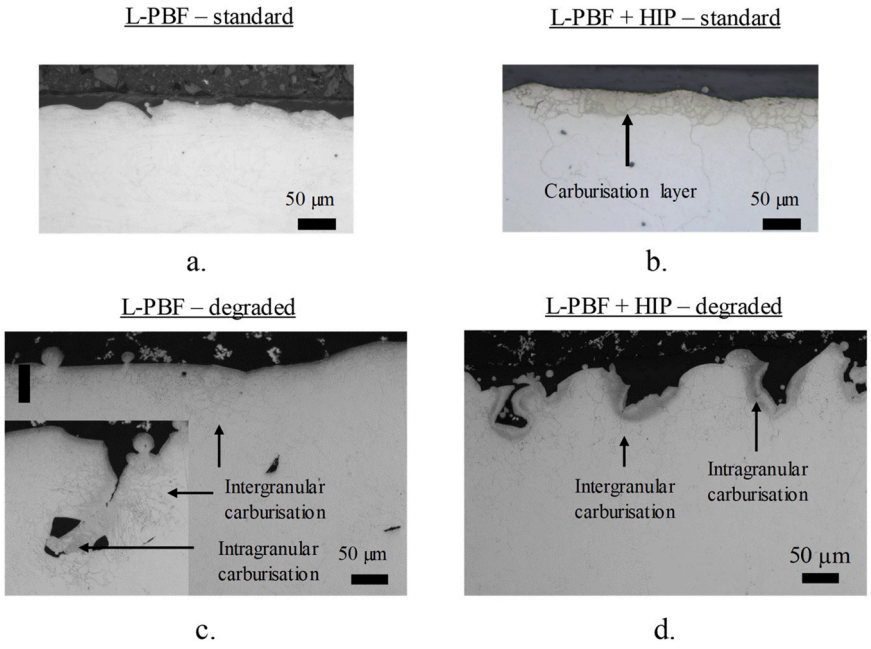

Fig. 10. OM image of the cross-sections of the four studied systems after 2 000 h of exposure to metal dusting and after Murakami's etching.

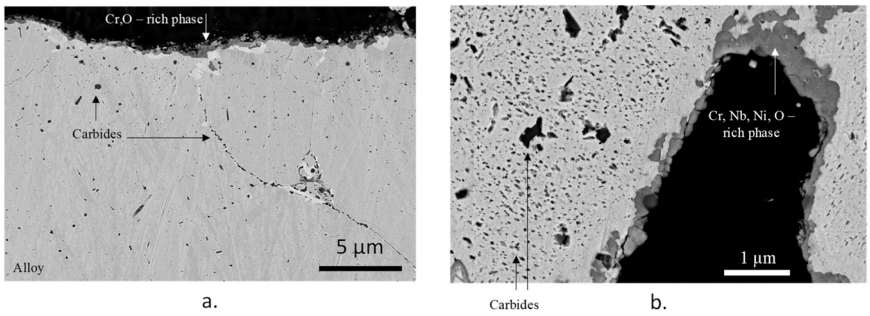

Fig. 11. SEM-BSE images of the cross-section of the L-PBF + HIP - degraded system a. in a defect-free area and b. in a defect after 2 000 h of exposure to the metal dusting atmosphere.

$$a_C = P_{CO} \times \frac{1}{\sqrt{P_{O2}}} \times \exp\left(\frac{-\Delta G_1}{RT}\right) \times \exp\left(\frac{-\Delta G_2}{RT}\right) \quad (8)$$

Eq. (8) demonstrates that when the oxygen partial pressure decreases it increases the carbon activity. This increased carbon activity in the gas can increase the C oversaturation and deposition of the carbon at the surface and its dissolution in the alloy.

The second hypothesis is that the observed pronounced carburisation around the defects is the result of the formation of a less protective oxide scale in these areas. As no protective oxide scale was observed by SEM before exposure to metal dusting on the surface of the defects and on defect free areas (Table 2), the carburisation observed after 2 000 h of metal dusting is the result of a competition between oxidation and carburisation in the first stages of the exposure to the metal dusting atmosphere [35]. The difference in the severity of the carburisation observed between defect and defect-free areas could be explained by the progressive formation of a protective oxide scale on the surface of the defect free areas, contrary to the defect areas where an unprotective oxide would form.

XRD surface analyses (Fig. 12) showed the presence of chromia and alumina on the surface of the sample obtained with degraded parameters after exposure to the metal dusting atmosphere. Raman spectroscopy confirmed this analysis (Fig. 13). No oxide was detected by XRD on the surface of the L-PBF+HIP - degraded system. However, this could be due to the presence of an oxide scale too thin to be detected by XRD. Raman spectroscopy and fluorescence of Cr^{3+} in alumina, which was more sensitive in our case, showed the presence of alumina, chromia and of a spinel oxide. The presence of a spinel oxide on the L-PBF + HIP sample explains the larger mass gain observed for this sample between 500 h and 1 500 h of exposure to the metal dusting atmosphere, compared to both the L-PBF system obtained with degraded parameters and the L-PBF+HIP obtained with standard parameters (Fig. 9). Indeed, spinel oxide, especially (Fe, Cr, Ni)$_3$O$_4$ spinel, is permeable to carbon [36,37]. The resulting increased carburisation would explain the higher mass gain.

To explain the enhanced carburisation around the alloy surface defects in comparison to defects free surface areas, the precise nature of the oxides on the defects and on the defect free areas needs to be determined. An oxide scale was observed by SEM observations on the defect-free area of the L-PBF + HIP sample, Fig. 11.a. Only Cr and O were detected by EDX, suggesting the presence of only chromia. From a chemical point of view, this oxide is protective against the metal dusting degradation but the scale is not continuous therefore allowing the

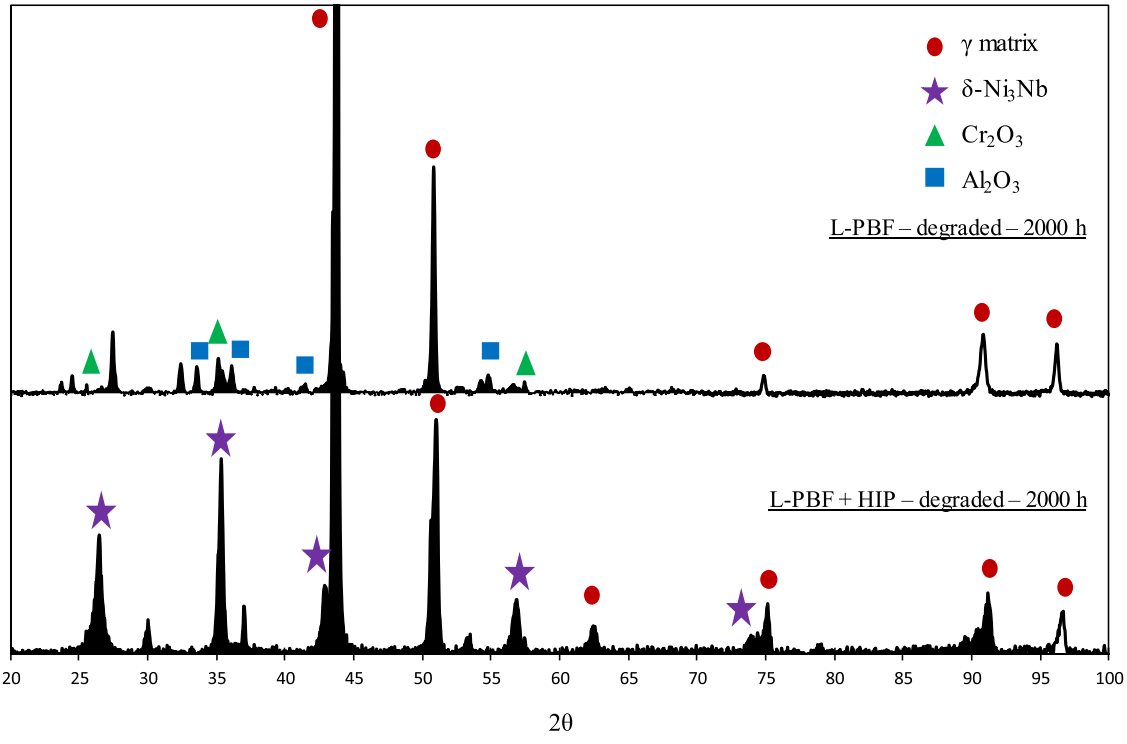

Fig. 12. XRD diffractograms of the L-PBF-degraded and L-PBF + HIP – degraded samples after 2 000 h of exposure to the metal dusting atmosphere.

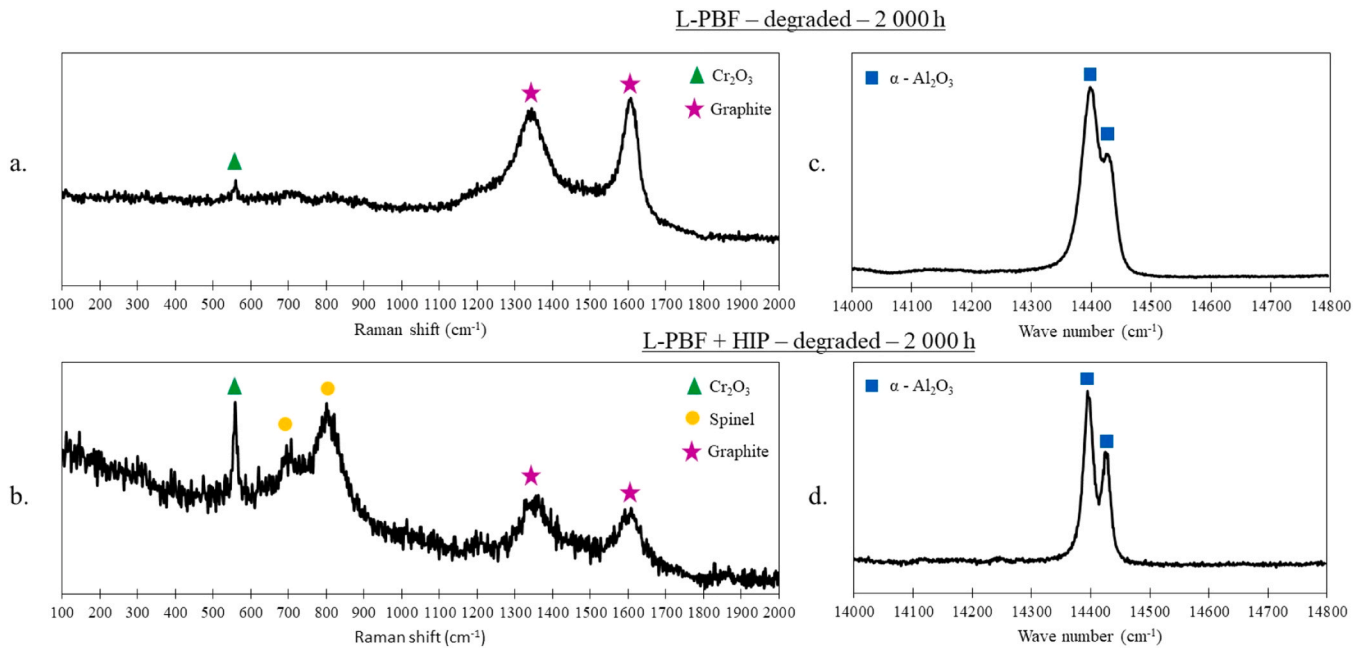

Fig. 13. (a) and (b) Raman spectroscopy and (c) and (d) fluorescence spectroscopy of the L-PBF - degraded and L-PBF + HIP – degraded samples after 2 000 h of exposure to the metal dusting atmosphere.

carburisation of the alloy. Nevertheless, the formation of chromia at the surface of the defect-free areas could decrease the number of adsorption sites for the carbonated molecules, explaining the less severe carburisation of the defect-free areas.

On the contrary, the oxide layer in the defects was composed of a mixed oxide (Cr, Nb, Ni)-rich, Fig. 11.b. TEM analyses were carried out to characterise more precisely the oxide formed on the surface of a defect (open pore). STEM-HAADF images coupled with EDX composition measurements show that the oxide scale was composed of two different oxides, one rich in Cr and another rich in Cr and Ni, Fig. 14.a. These two phases were identified by electron diffraction as hexagonal chromia and a tetragonal $NiCr_2O_4$ respectively. This tetragonal phase is not usually observed after exposure to metal dusting atmospheres. It was only detected between −183 and 77 °C by Mikheykin *et al.* using synchrotron X-ray powder diffraction [38]. The crystallographic structure evolves from cubic above approximately 70 °C to tetragonal during cooling due to a distortion of the crystal called the Jahn-Teller effect [38]. It is therefore possible that this particular structure formed during cooling and not during exposure to the metal dusting atmosphere. Ni particles were also detected within the oxide scale and at the surface. If the oxygen partial pressure decreases in an open pore, as explained before, $NiCr_2O_4$ can be partially reduced and metallic Ni nanoparticles can form [7]. These metallic particles catalyse the decomposition of the carbon-rich molecules. Moreover, Grabke showed that a spinel oxide is permeable to carbon [39] and Gheno *et al.* that carbon activity increases beneath the external oxide scale due to the oxygen activity gradient in the oxide scale [40]. The combination of these two phenomena may explain the formation of carbides under the $NiCr_2O_4$ oxide. It is interesting to note that directly beneath the oxide scale (Fig. 11.b) no carbide is formed. This carbide-free layer is approximately 250 nm thick. This can be explained by the Cr depletion under the oxide scale observed on the STEM-EDX mapping of Cr (Fig. 14.a) which prevents carbide formation under the oxide scale. This is a classic observation during carburisation of chromia forming alloys [41,42]. Moreover a previous study showed by thermodynamic calculations that the volume fraction of chromium carbides in a Cr-depleted matrix is inferior to the volume fraction of carbides in a non-depleted matrix [12]. It also showed that the carbon solubility is lower in a Cr-depleted matrix, reducing the carburisation of the alloy.

From this information it can be supposed that the initial competition between oxidation and carburisation resulted in the intergranular carburisation observed below the surface of the whole sample. However, the formation of a non-continuous chromia scale on the surface of the defect-free areas could have slowed down the carburisation in these areas. On the contrary, the oxide scale that formed at the surface of the defects was not protective (Cr_2O_3 and $NiCr_2O_4$ mix): the carburisation was not slowed down, resulting in the intragranular carburisation observed in the alloy matrix around the alloy defects.

The third and last hypothesis that could explain the more severe metal dusting degradation in the defects is a faster diffusion of C due to a finer microstructure. A fine microstructure is usually said to favour Cr diffusion towards the surface. In our study, no continuous chromia scale was observed by SEM or TEM on the surface of the open pores of the alloy. Carburisation of the alloy therefore occurred and the carbon diffusion could have been enhanced by the fine microstructure. The microstructure is indeed thinner in the defects than in the defect free areas for the L-PBF – degraded sample but this is not observed for the L-PBF + HIP –degraded where the enhanced carburisation of the defects is particularly observed. It therefore seems unlikely that the grain size has an influence on the metal dusting degradation observed in this study. Note that the finer microstructure observed in the defects of the degraded system, Fig. 8, does not lead to a sufficient increase in the flux of Cr to form a continuous chromia scale on the surface.

5. Conclusion

The effect of additive manufacturing processing parameters such as contouring, laser scanning speed and hatching distance was studied during 4 000 h in a 48%H_2-9%CO-6%CO_2-3%CH_4-34%H_2O atmosphere at 610 °C, with $a_C = 6.9$ and $P_{O2} = 1.8 \times 10^{-24}$ bar. Several conclusions can be drawn:

- A higher scanning velocity and hatching distance as well as the lack of contouring resulted in the formation of numerous surface defects and in a larger surface roughness (approximately 3 times larger) which increased the surface area of the alloy in contact with the metal dusting atmosphere.

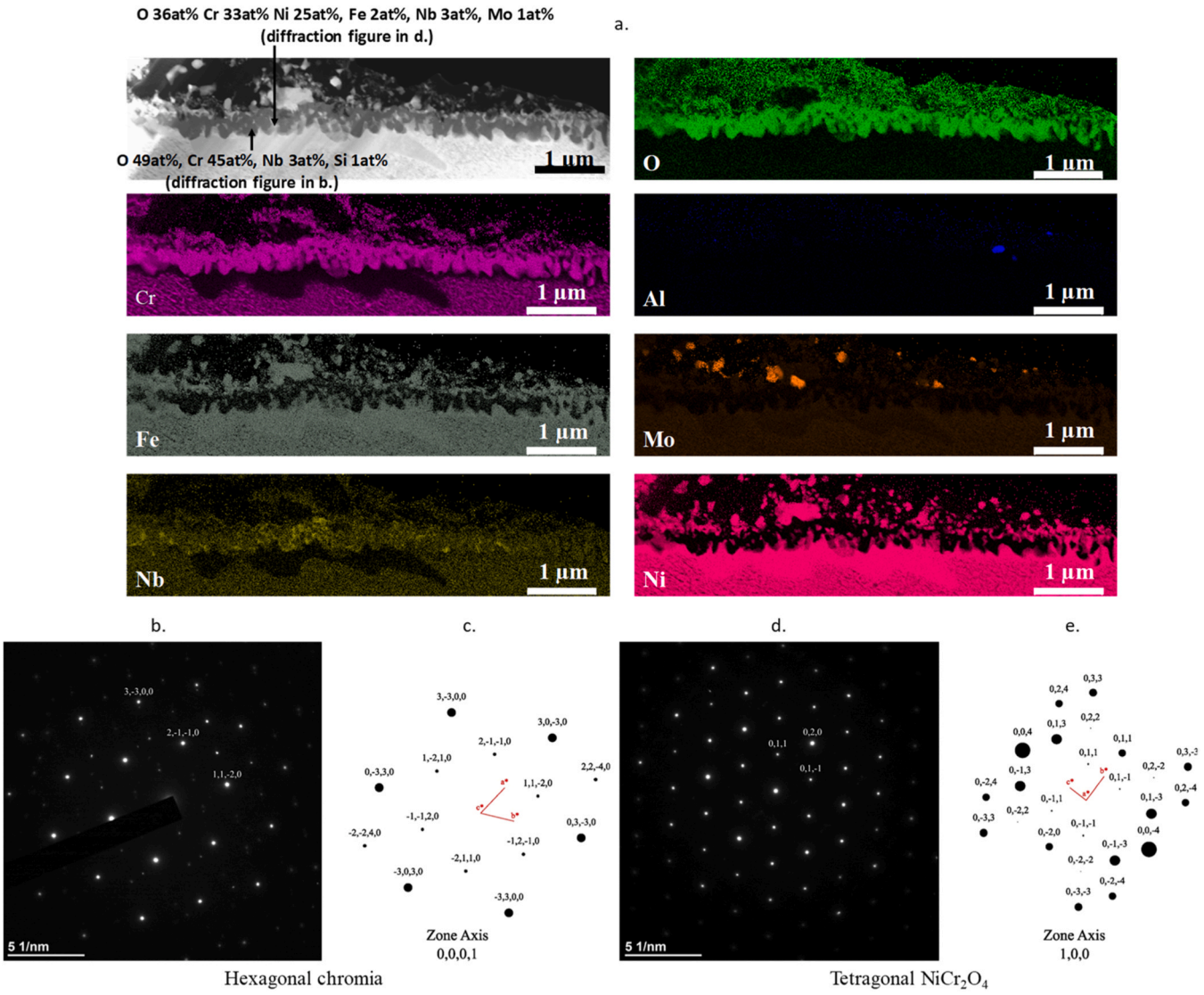

Fig. 14. TEM analyses of an area of a FIB lamella of the L-PBF + HIP - degraded system taken at the bottom of a defect, a. STEM-HAADF image and STEM-EDX mapping, b. and d. SAED pattern of the marked zones in STEM-HAADF image of Fig. 14.a, c. and e. theoretical electron diffraction [43] of hexagonal chromia and tetragonal $NiCr_2O_4$ [38].

- The HIP treatment performed after fabrication eliminates the internal porosity and surprisingly slightly decreases the number of surface defects (open porosity).
- The oxides formed during HIP treatment varied according to the batch of samples. Samples obtained using standard parameters presented locally some alumina whereas samples fabricated with degraded parameters presented locally chromia and alumina as well as internal oxidation (likely alumina). However, samples obtained with optimised parameters (no surface defects) also presented internal oxidation. Therefore, the surface defects do not have an influence on the presence of internal oxidation. This underlines the lack of control of gaseous species activities during an industrial HIP treatment, as pointed out by [29].
- Samples obtained with degraded parameters exhibited a significantly smaller incubation time than the ones fabricated with standard parameters (1 000 h compared to about 6 500 h) for both the L-PBF and L-PBF + HIP systems. The first pit also appeared much earlier in the case of the samples obtained with degraded parameters (1 500 h compared to 3 000 h for one L-PBF + HIP standard sample and 6 500 h for the rest of the standard samples).
- Carburisation was not observed after 2 000 h on the L-PBF - standard system and was homogeneous on the L-PBF + HIP - standard system. For the L-PBF degraded system, carburisation was present after 2 000 h and more pronounced in the defects. For the L-PBF + HIP system obtained with degraded parameters, intergranular carburisation below the surface was observed on the whole sample and intragranular carburisation was observed in the alloy surface defects. The defects enhanced the carburisation of the alloy.
- The maximum depth of carburisation that was observed was consistent with a diffusion calculation taking into account the consumption of carbon during the precipitation of $M_{23}C_6$ and the blocking effect of the precipitates for the inward flux of carbon in the gamma matrix.
- The defect-free areas (no open pores/lacks of fusion) at the surface of the L-PBF - degraded samples presented more carburisation than the L-PBF - standard samples because of the lower dislocation density of the samples obtained with degraded parameters. The surface defects are not the only reason for the poor metal dusting resistance of the samples fabricated with degraded process parameters, the resulting microstructure of the alloy is also a factor.

- Several hypotheses were made to explain the more pronounced carburisation around defects (open pores) at the alloy surface. The confined atmosphere created by the defect could induce the decrease in the oxygen partial pressure and consequently the increase in the local carbon oversaturation and deposition on the alloy. The decrease in oxygen activity can also partially reduce oxides containing Ni cations, forming metallic Ni particle which catalyses the decomposition of C-rich molecules. Therefore more carbon could have been available to form carbides. The oxides formed in the defects are chromia as well as a non-protective oxide $NiCr_2O_4$ which could also explain the enhanced carburisation in this area.

Declaration of Competing Interest

The authors declare that they have no known competing financial interests or personal relationships that could have appeared to influence the work reported in this paper.

Data availability

The authors do not have permission to share data.

Acknowledgments

Authors would like to thank BPI France for financial support of the FAIR project and Air Liquide for helpful discussions and technical support. The authors would also like to warmly thank Claudie Josse and Arnaud Projetti of Raimond Castaing Microanalysis Center for their helpful contribution to the TEM lamella preparation and EBSD analysis, respectively.

References

[1] E.Q. Camp, C. Phillips, L. Gross, Corrosion of 18-8 alloy furnace tubes in high-temperature vapor phase cracking service, Corrosion 1 (1945) 149–160, https://doi.org/10.5006/0010-9312-1.3.149.
[2] F.A. PRANGE, Mechanical properties and corrosion resistance of oil well tubing, Corrosion 15 (1959) 13–18, https://doi.org/10.5006/0010-9312-15.2.13.
[3] D. Young, J. Zhang, C. Geers, M. Schütze, Recent advances in understanding metal dusting: a review, Mater. Corros. 62 (2011) 7–28, https://doi.org/10.1002/maco.201005675.
[4] A. Agüero, M. Gutiérrez, L. Korcakova, T. Nguyen, B. Hinnemann, S. Saadi, Metal dusting protective coatings. A literature review, Oxid. Met. 76 (2011) 23–42, https://doi.org/10.1007/s11085-011-9248-4.
[5] H. Taheri, M. Shoaib, L. Koester, T. Bigelow, P. Collins, L. Bond, Powder-based additive manufacturing-a review of types of defects, generation mechanisms, detection, property evaluation and metrology, Int. J. Addit. Subtractive Mater. Manuf. 1 (2017) 172–209, https://doi.org/10.1504/IJASMM.2017.10009247.
[6] W.J. Sames, F.A. List, S. Pannala, R.R. Dehoff, S.S. Babu, The metallurgy and processing science of metal additive manufacturing, Int. Mater. Rev. 61 (2016) 315–360, https://doi.org/10.1080/09506608.2015.1116649.
[7] D.J. Young, Metal dusting reaction mechanisms, Mater. Sci. Forum 522–523 (2006) 15–26, https://doi.org/10.4028/www.scientific.net/MSF.522-523.15.
[8] A. Fabas, A. Rouaix-Vande Put, S. Doublet, D. Domergue, M. Salem, D. Monceau, Metal dusting corrosion of austenitic alloys at low and high pressure with the effects of Cr, Al, Nb and Cu, Corros. Sci. 123 (2017) 310–318, https://doi.org/10.1016/j.corsci.2017.04.015.
[9] C. Hong, D. Gu, D. Dai, S. Cao, M. Alkhayat, Q. Jia, A. Gasser, A. Weisheit, I. Kelbassa, M. Zhong, R. Poprawe, High-temperature oxidation performance and its mechanism of TiC/Inconel 625 composites prepared by laser metal deposition additive manufacturing, J. Laser Appl. 27 (2014) S17005, https://doi.org/10.2351/1.4898647.
[10] K. Pineda-Arriaga, J. Ramírez-Ramírez, F. Pérez-González, J. Alvardo-Orozco, R. Colás, N. Garza-Montes-de-Oca, Characterization of the high temperature oxidation behaviour of Inconel 625 ® fabricated by additive manufacturing and conventional method, (2022). https://doi.org/10.21203/rs.3.rs-1728294/v1.
[11] T. Sanviemvongsak, D. Monceau, B. Macquaire, High temperature oxidation of IN 718 manufactured by laser beam melting and electron beam melting: effect of surface topography, Corros. Sci. 141 (2018) 127–145, https://doi.org/10.1016/j.corsci.2018.07.005.
[12] A. Vernouillet, A. Vande Put, A. Pugliara, S. Doublet, D. Monceau, Metal dusting of Inconel 625 obtained by laser beam melting: effect of manufacturing process and hot isostatic pressure treatment, Corros. Sci. 174 (2020) 108820, https://doi.org/10.1016/j.corsci.2020.108820.
[13] D. Monceau, M. Vilasi, High temperature oxidation of additively manufactured structural alloys, JOM 74 (2022) 1659–1667, https://doi.org/10.1007/s11837-022-05198-z.
[14] N.H. Sateesh, G.C.M. Kumar, K. Prasad, S.C. kVinod, Microstructure and mechanical characterization of laser sintered Inconel-625 superalloy, Procedia Mater. Sci. 5 (2014) 772–779, https://doi.org/10.1016/j.mspro.2014.07.327.
[15] E. Louvis, P. Fox, C.J. Sutcliffe, Selective laser melting of aluminium components, J. Mater. Process. Technol. 211 (2011) 275–284, https://doi.org/10.1016/j.jmatprotec.2010.09.019.
[16] Q. Jia, D. Gu, Selective laser melting additive manufactured Inconel 718 superalloy parts: High-temperature oxidation property and its mechanisms, Opt. Laser Technol. 62 (2014) 161–171, https://doi.org/10.1016/j.optlastec.2014.03.008.
[17] N. Ramenatte, A. Vernouillet, S. Mathieu, A. Vande Put, M. Vilasi, D. Monceau, A comparison of the high-temperature oxidation behaviour of conventional wrought and laser beam melted Inconel 625, Corros. Sci. 164 (2020) 108347, https://doi.org/10.1016/j.corsci.2019.108347.
[18] T. Sanviemvongsak, D. Monceau, C. Desgranges, B. Macquaire, Intergranular oxidation of Ni-base alloy 718 with a focus on additive manufacturing, Corros. Sci. 170 (2020) 108684, https://doi.org/10.1016/j.corsci.2020.108684.
[19] C. Juillet, A. Oudriss, J. Balmain, X. Feaugas, F. Pedraza, Characterization and oxidation resistance of additive manufactured and forged IN718 Ni-based superalloys, Corros. Sci. 142 (2018) 266–276, https://doi.org/10.1016/j.corsci.2018.07.032.
[20] T. De Terris, Fabrication additive par fusion laser sélective (SLM) d'un superalliage base nickel: relations procédé – microstructures – propriétés mécaniques., These de doctorat, Paris, ENSAM, 2019. https://theses.fr/2019ENAM0061 (accessed January 29, 2024).
[21] C. Chun, G. Bhargava, T. Ramanarayanan, Metal dusting corrosion of nickel-based alloys, ECS Trans. 3 (2007) 43, https://doi.org/10.1149/1.2721458.
[22] T.A. Ramanarayanan, C. Chun, Metal dusting corrosion: mechanisms and control, ECS Trans. 41 (2012) 47, https://doi.org/10.1149/1.4717999.
[23] D. Young, High Temperature Oxidation and Corrosion of Metals, Elsevier, 2016.
[24] A. Engström, L. Höglund, J. Ågren, Computer simulation of diffusion in multiphase systems, Metall. Mater. Trans. A 25 (1994) 1127–1134, https://doi.org/10.1007/BF02652288.
[25] F. Xu, Y. Lv, Y. Liu, B. Xu, P. He, Effect of heat treatment on microstructure and mechanical properties of Inconel 625 alloy fabricated by pulsed plasma arc deposition, Phys. Procedia 50 (2013) 48–54, https://doi.org/10.1016/j.phpro.2013.11.010.
[26] F. Zhang, L.E. Levine, A.J. Allen, C.E. Campbell, E.A. Lass, S. Cheruvathur, M. R. Stoudt, M.E. Williams, Y. Idell, Homogenization kinetics of a nickel-based superalloy produced by powder bed fusion laser sintering, Scr. Mater. 131 (2017) 98–102, https://doi.org/10.1016/j.scriptamat.2016.12.037.
[27] T.M. Besmann, N.S. Kulkarni, K.E. Spear, Thermochemical analysis and modeling of the Al2O3–Cr2O3, Cr2O3–SiO2, and Al2O3–Cr2O3–SiO2 systems relevant to refractories, J. Am. Ceram. Soc. 89 (2006) 638–644, https://doi.org/10.1111/j.1551-2916.2005.00719.x.
[28] J.-W. Park, C.J. Altstetter, The diffusion and solubility of oxygen in solid nickel, Metall. Trans. A 18 (1987) 43–50, https://doi.org/10.1007/BF02646220.
[29] N. Mrozowski, A. Prillieux, E. Erica, C. Desgranges, Hugues, D. Monceau, Surface reactivity during an Hot Isostatic Pressing treatment of Ni-based superalloy René 77 specimens manufactured by Laser Powder Bed Fusion and Metal Inject Molding, Corrosion Science, in press (2024).
[30] Y.L. Hu, X. Lin, S.Y. Zhang, Y.M. Jiang, X.F. Lu, H.O. Yang, W.D. Huang, Effect of solution heat treatment on the microstructure and mechanical properties of Inconel 625 superalloy fabricated by laser solid forming, J. Alloy. Compd. 767 (2018) 330–344, https://doi.org/10.1016/j.jallcom.2018.07.087.
[31] Y.-L. Kuo, T. Nagahari, K. Kakehi, The effect of post-processes on the microstructure and creep properties of alloy718 built up by selective laser melting, Mater. Basel Switz. 11 (2018) 996, https://doi.org/10.3390/ma11060996.
[32] W.M. Tucho, V. Hansen, Characterization of SLM-fabricated Inconel 718 after solid solution and precipitation hardening heat treatments, J. Mater. Sci. 54 (2019) 823–839, https://doi.org/10.1007/s10853-018-2851-x.
[33] T. De Terris, O. Castelnau, Z. Hadjem-Hamouche, H. Haddadi, V. Michel, P. Peyre, Analysis of as-built microstructures and recrystallization phenomena on Inconel 625 alloy obtained via laser powder bed fusion (L-PBF), Metals 11 (2021) 619, https://doi.org/10.3390/met11040619.
[34] A. Fabas, D. Monceau, C. Josse, P. Lamesle, A. Rouaix-Vande Put, Mechanism of metal dusting corrosion by pitting of a chromia-forming alloy at atmospheric pressure and low gas velocity, Corros. Sci. 107 (2016) 204–210, https://doi.org/10.1016/j.corsci.2016.02.033.
[35] H.J. Grabke, E.M. Muller-Lorenz, S. Strauss, E. Pippel, J. Woltersdorf, Effects of grain size, cold working, and surface finish on the metal-dusting resistance of steels, Oxid. Met 50 (1998) 241–254, https://doi.org/10.1023/A:1018888321213.
[36] H.J. Grabke, K. Ohla, J. Peters, I. Wolf, Radiotracer studies of carbon permeation through oxide scales on commercial high temperature alloys and model alloys, Mater. Corros. 34 (1983) 495–500, https://doi.org/10.1002/maco.19830341002.
[37] D. Röhnert, F. Phillipp, H. Reuther, T. Weber, E. Wessel, M. Schütze, Initial stages in the metal-dusting process on alloy 800, Oxid. Met. 68 (2007) 271–293, https://doi.org/10.1007/s11085-007-9075-9.
[38] A. Mikheykin, D. Chernyshov, A. Bush, A. Prokhorov, Y. Yuzyuk, V. Dmitriev, Features of the Jahn-Teller transition in Ni1 − x Co x Cr2O4 solid solutions, Phys. Solid State 56 (2014) 785–791, https://doi.org/10.1134/S1063783414040209.
[39] H.J. Grabke, Metal dusting, Mater. Corros. 54 (2003) 736–746, https://doi.org/10.1002/maco.200303729.

[40] T. Gheno, D. Monceau, J. Zhang, D.J. Young, Carburisation of ferritic Fe–Cr alloys by low carbon activity gases, Corros. Sci. 53 (2011) 2767–2777, https://doi.org/10.1016/j.corsci.2011.05.013.
[41] T. Gheno, D. Monceau, D.J. Young, Mechanism of breakaway oxidation of Fe–Cr and Fe–Cr–Ni alloys in dry and wet carbon dioxide, Corros. Sci. 64 (2012) 222–233, https://doi.org/10.1016/j.corsci.2012.07.024.
[42] N. Xu, D. Monceau, D. Young, J. Furtado, High temperature corrosion of cast heat resisting steels in CO+CO2 gas mixtures, Corros. Sci. 50 (2008) 2398–2406, https://doi.org/10.1016/j.corsci.2008.06.001.
[43] Ca.R.Ine Cristallographie- UTeam, (n.d.). https://uteam.fr/offres/carine-cristallographie (accessed July 16, 2023).